Adaptive Linear Quadratic Gaussian Optimal Control Modification for Flutter Suppression of Adaptive Wing

Nhan T. Nguyen*
NASA Ames Research Center, Moffett Field, CA 94035
Sean Swei†
NASA Ames Research Center, Moffett Field, CA 94035
Eric Ting ‡
Stinger Ghaffarian Technologies Inc., Moffett Field, CA 94035

This paper presents an adaptive control approach for flutter suppression of a performance adaptive aeroelastic wing equipped with a variable camber continuous trailing edge flap design. The adaptive control approach is based on the optimal control modification method augmented to a linear quadratic gaussian optimal control design. A model reduction based on a singular perturbation approach is presented. The control surfaces are subject to relative motion constraints due to the elastomer transition material in between the flap sections. A virtual control method is proposed using a shape function to deal with the relative motion constraints. Simulation results indicate that the adaptive augmentation control design is effective in suppressing unstable aeroelastic modes.

I. Introduction

The aircraft industry has been responding to the need for energy-efficient aircraft by redesigning airframes to be aerodynamically efficient, employing light-weight materials for aircraft structures and incorporating more energy-efficient aircraft engines. Reducing airframe operational empty weight (OEW) using advanced composite materials is one of the major considerations for improving energy efficiency. Modern light-weight materials can provide less structural rigidity while maintaining sufficient load-carrying capacity. As structural flexibility increases, aeroelastic interactions with aerodynamic forces and moments can alter aircraft aerodynamics significantly, thereby potentially degrading aerodynamic efficiency.

Under the Fundamental Aeronautics Program in NASA Aeronautics Research Mission Directorate, the Fixed Wing project is conducting multidisciplinary research to investigate advanced concepts and technologies for future aircraft systems. A NASA study entitled "Elastically Shaped Future Air Vehicle Concept" was conducted in 2010[1,2] to examine new concepts that can enable active control of wing aeroelasticity to achieve drag reduction. This study shows that highly flexible wing aerodynamic surfaces can be elastically shaped in-flight by active control of wing twist and vertical deflection in order to optimize the local angles of attack of wing sections to improve aerodynamic efficiency through drag reduction during cruise and enhanced lift performance during take-off and landing.

*Research Scientist, Intelligent Systems Division, nhan.t.nguyen@nasa.gov, AIAA Associate Fellow
†Research Scientist, Intelligent Systems Division, sean.s.swei@nasa.gov
‡Stinger Ghaffarian Technologies Inc., NASA Ames Research Center, Research Engineer, eric.b.ting@nasa.gov

The study shows that active aeroelastic wing shaping control can have a potential drag reduction benefit. Conventional flap and slat devices inherently generate drag as they increase lift. The study shows that conventional flap and slat systems are not aerodynamically efficient for use in active aeroelastic wing shaping control for drag reduction. A new flap concept, referred to as Variable Camber Continuous Trailing Edge Flap (VCCTEF) system, was conceived by NASA to address this need.[1] Initial study results indicate that, for some applications, the VCCTEF system may offer a potential pay-off in drag reduction that could provide significant fuel savings. In order to realize the potential benefit of drag reduction by active span-load and aeroelastic wing shaping control while meeting all other performance requirements, the approach for high lift devices needs to be considered as part of the wing shaping control strategy.

NASA and Boeing are currently conducting a joint study to develop the VCCTEF further under the research element Active Aeroelastic Shape Control (AASC) within the Fixed Wing project.[3,4] This study is built upon the development of the VCCTEF system for NASA Generic Transport Model (GTM) which is essentially based on the Boeing 757 airframe, employing light-weight shaped memory alloy (SMA) technology for actuation and three separate chordwise segments shaped to provide a variable camber to the flap. This cambered flap has potential for drag reduction as compared to a conventional straight, plain flap. The flap is also made up of individual 2-foot spanwise sections which enable different flap setting at each flap spanwise position. This results in the ability to control the wing twist shape as a function of span, resulting in a change to the wing twist to establish the best lift-to-drag ratio (L/D) at any aircraft gross weight or mission segment. Wing twist on traditional commercial transport designs is dictated by the aeroelastic deflection of a fixed "jig twist" shape applied at manufacture. The design of this jig twist is set for one cruise configuration, usually for a 50% fuel loading or mid-point on the gross weight schedule. The VCCTEF offers different wing twist settings, hence different spanwise loadings, for each gross weight condition and also different settings for climb, cruise and descent, a major factor in obtaining best L/D conditions.

The second feature of VCCTEF is a continuous trailing edge flap. The individual 2-foot spanwise flap sections are connected with a flexible covering, so no breaks can occur in the flap planforms, thus reducing drag by eliminating these breaks in the flap continuity which otherwise would generate vorticity that results in a drag increase and also contributes to airframe noise. This continuous trailing edge flap design combined with the flap camber result in lower drag increase during flap deflections. In addition, it also offers a potential noise reduction benefit.

The VCCTEF is divided into 14 sections attached to the outer wing and 3 sections attached to the inner wing, as shown in Fig. 1.[4] Each 24-inch section has three camber flap segments that can be individually commanded to form a variable camber trailing edge, as shown in Fig. 2. These camber flaps are joined to the next section by a flexible and supported material (shown in blue) installed with the same shape as the camber and thus providing continuous flaps throughout the wing span with no drag producing gaps.

Using the camber positioning, a full-span, low-drag, high-lift configuration can be activated that has no drag producing gaps and a low flap noise signature. This is shown in Fig. 3. To further augment lift, a slotted flap configuration is formed by an air passage between the wing and the inner flap that serves to improve airflow over the flap and keep the flow attached. This air passage appears only when the flaps are extended in the high lift configuration.

Figure 4 illustrates the GTM equipped with the VCCTEF for wing shaping control. By actively shaping the wing aerodynamic surface using the VCCTEF, optimal aerodynamic performance could potentially be realized at any point in the flight envelope. The VCCTEF relies on two mechanisms to improve aerodynamic performance: 1) wing twist optimization for flexible wing design, and 2) variable camber and continuous trailing edge for improved aerodynamics. This fixed-wing technology may be referred to as Performance Adaptive Aeroelastic Wing (PAAW) technology.

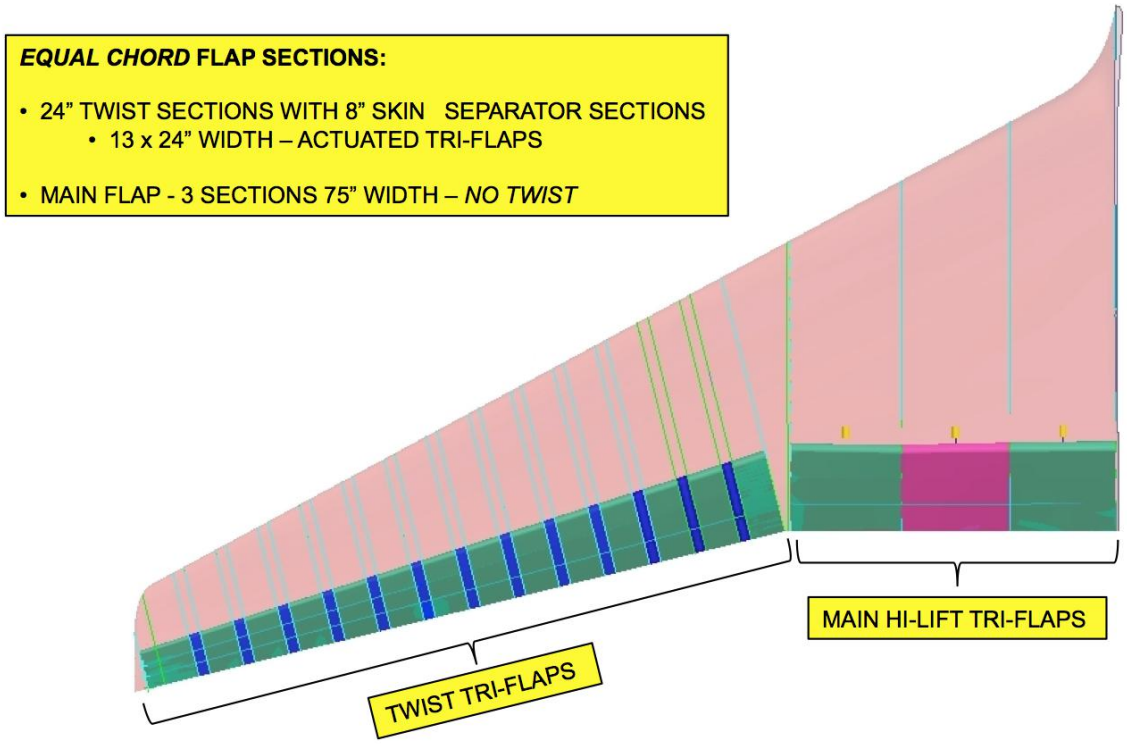

Fig. 1 - Wing Configured with the Variable Camber Continuous Trailing Edge Flap

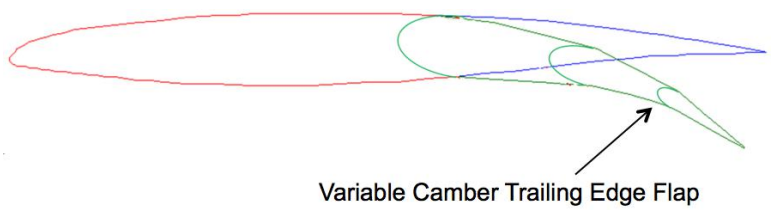

Fig. 2 - Variable Camber Flap

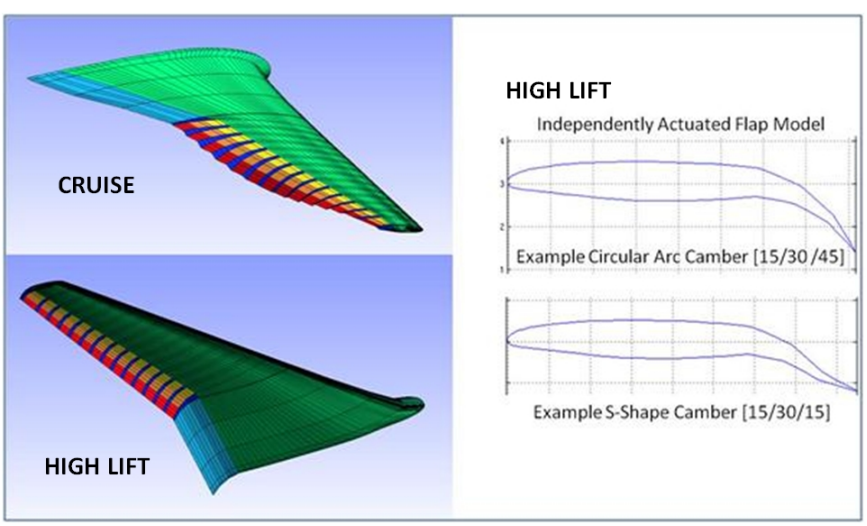

Fig. 3 - Cruise and High Lift VCCTEF Configurations

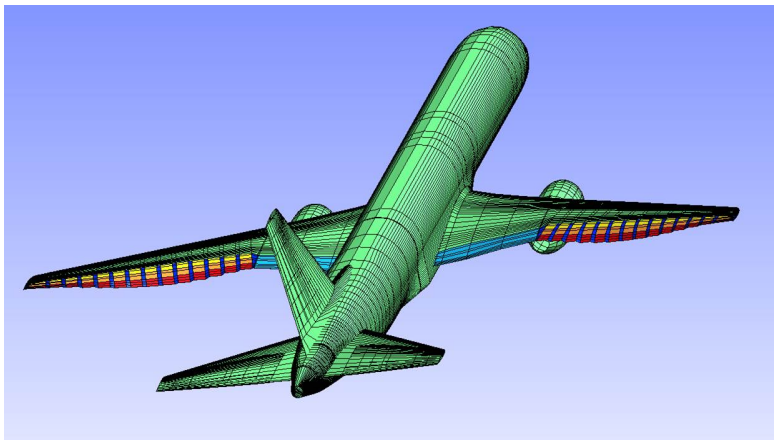

Fig. 4 - GTM with VCCTEF

The performance of an adaptive wing can be described by the following equation:[5]

$$\alpha_c(y) = \alpha\left[1 - \frac{\partial\Theta(\bar{y})}{\partial\alpha}\cos\Lambda - \frac{\partial}{\partial\alpha}\left(\frac{dW(\bar{y})}{d\bar{y}}\right)\sin\Lambda\right] - \alpha_i(y) - \gamma(\bar{y})\cos\Lambda - \Theta_0(\bar{y})\cos\Lambda - \frac{dW_0(\bar{y})}{d\bar{y}}\sin\Lambda$$
$$+\sum_{i=1}^{N}\left[\frac{\partial\alpha_c}{\partial\delta_i}\cos\Lambda_h - \frac{\partial\Theta(\bar{y})}{\partial\delta_i}\cos\Lambda - \frac{\partial}{\partial\delta_i}\left(\frac{dW(\bar{y})}{d\bar{y}}\right)\sin\Lambda\right]\delta(y_h) \tag{1}$$

where α_c is the sectional angle of attack, α is the geometric angle of attack of the wing section about the pitch axis y, α_i is the induced angle of attack due to the downwash about the pitch axis y, γ is the wing pre-twist angle about the elastic axis $\bar{y} = y/\cos\Lambda$ (positive nose down), Θ is the wing torsional twist about the elastic axis $\bar{y}$ (positive nose down), W is wing vertical bending along the elastic axis (positive upward), Λ is the sweep angle of the elastic axis, δ_i is the absolute deflection of the i-th flap segment of the VCCTEF about the hinge axis y_h which has a sweep angle of Λ_h, and $\partial\alpha_c/\partial\delta_i$ is the angle of attack sensitivity or camber control derivative due to the VCCTEF flap deflection.

It can be seen that the aeroelastic deflections can cause the desired sectional angle of attack to be non-optimal. The effect of the adaptive aeroelastic wing shaping control by the VCCTEF is captured in the last term. The term $\partial\alpha_c/\partial\delta_i$ is the rigid camber control to compensate for the non-optimal sectional angle of attack. The two terms $\partial\Theta/\partial\delta_i$ and $\partial(dW/d\bar{y})/\partial\delta_i$ are the aeroelastic wing shaping control by leveraging wing flexibility to change the wash-out twist of a wing in order to achieve improved aerodynamic performance. Thus, the effect of adaptive aeroelastic wing shaping control is to optimize the span load at any operating point inside a given flight envelope.

The flexibility of modern transport wings can cause a reduction in flutter margins which can compromise stability of aircraft. In a previous study, a flutter analysis was conducted to examine the effect of increased flexibility of the GTM wing.[6] The baseline wing stiffness of the GTM is reduced by 50%. This wing is referred to as the Elastic Shaped Aircraft Concept (ESAC) wing. Table 1 shows the flutter speed prediction at 35,000 ft for the GTM wing and the ESAC wing. The critical flutter modes for the GTM wing and ESAC wing are the first anti-symmetric bending mode. The flutter speed prediction is also compared against NASTRAN doublet lattice solution which gives a flutter speed of Mach 0.954 for the ESAC wing at 35,000 ft corresponding to the first anti-symmetric bending mode at a frequency of 2.53 Hz. This represents a 3% difference which demonstrates an excellent agreement.

	Symmetric Mode	Anti-Symmetric Mode
GTM Flutter Mach @ 35K ft	1.358	1.310
GTM Flutter Frequency @ 35K ft, Hz	4.31	3.87
ESAC Flutter Mach @ 35K ft	0.938	0.925
ESAC Flutter Frequency @ 35K ft, Hz	6.94	2.85

Table 1 - Flutter Speed Prediction

The FAA certification requires a flutter margin of at least 15% above the dive speed which is normally determined from flight testing. For a maximum operating Mach 0.8, the dive speed may be estimated at 20% over the maximum operating Mach, or 0.96. Thus, the flutter clearance requires a flutter speed of at least Mach 1.10 at 35,000 ft. The GTM wing demonstrates to meet this flutter clearance but not the ESAC wing. Thus, active flutter suppression control will be required. In practice, active flutter suppression could be difficult to certify since aircraft must demonstrate to be open-loop stable. Also, active flutter suppression control will require power which could offset any potential aerodynamic performance benefits from wing shaping control using the VCCTEF.

To address the wing shaping control objective, a multidisciplinary design analysis optimization (MDAO) framework must be considered by incorporating the aerodynamic performance prediction together with aeroelasticity and flutter suppression control. The objective of the MDAO is to identify a desired wing flexibility that would provide the best overall aerodynamic, aeroelasticity, and control benefits. For example, the wing stiffness could be reduced to an optimal value that would maximize the aerodynamic performance at off-design cruise with the least amount of control effort to maintain aeroelastic stability margin. The MDAO would also include control gain synthesis directly in the MDAO process.

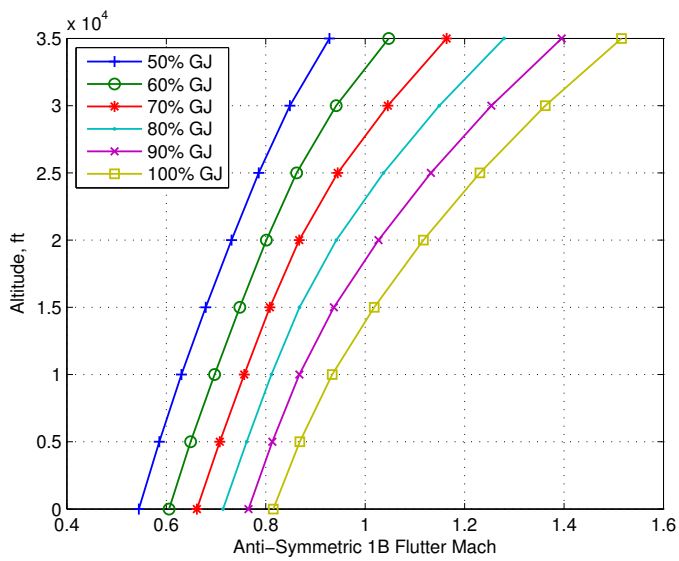

Fig. 5 - Flutter Boundary of ESAC Wing as a Function of *GJ*

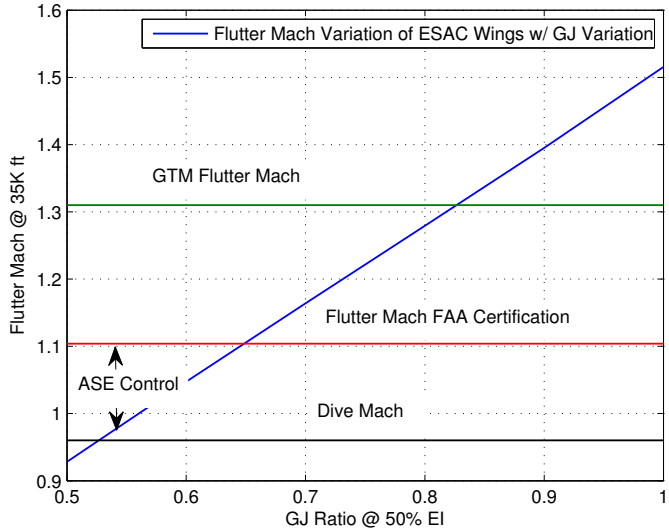

Fig. 6 - Flutter Mach Clearance of ESAC Wing

To explore the effect of stiffness reduction on the flutter speed, a sensitivity study is conducted to determine the flutter boundary as a function of the ESAC wing torsional stiffness GJ while the ESAC wing bending stiffness EI is kept at half of that of the GTM wing. Figure 5 is a plot that shows the flutter boundary for a varying torsion stiffness from 100% to 50% of that of the GTM wing. It can be seen from Fig. 6 that to clear the flutter boundary at Mach 1.1, the ESAC wing torsional stiffness GJ cannot be reduced to less than 65% of that of the GTM wing. The question to be investigated is whether or not there are any aerodynamic performance benefits to reduce torsional stiffness GJ further in exchange for the need to incorporate active flutter suppression control.

This paper presents a study of a candidate adaptive flutter suppression control. The adaptive control method is the Optimal Control Modification designed as an adaptive augmentation control to a baseline control which uses a Linear Quadratic Gaussian (LQG) method. The aeroelastic state space models were generated by NASTRAN for various flight conditions for the ESAC wing. The four outboard third camber flap segment of the VCCTEF are used as control inputs. A model reduction is developed using the singular perturbation method for control design.

II. Aeroelastic State Space Model Reduction

Consider a general aeroservoelastic (ASE) state space model of the form

$$\begin{bmatrix} \dot{\eta} \\ \dot{\mu} \end{bmatrix} = \begin{bmatrix} A_{11} & A_{12} \\ A_{21} & A_{22} \end{bmatrix} \begin{bmatrix} \eta \\ \mu \end{bmatrix} + \begin{bmatrix} B_{11} & B_{12} & B_{13} \\ B_{21} & B_{22} & B_{23} \end{bmatrix} \begin{bmatrix} \delta \\ \dot{\delta} \\ \ddot{\delta} \end{bmatrix} \tag{2}$$

$$y = C_1\eta + C_2\mu + D_1\delta + D_2\dot{\delta} + D_3\ddot{\delta} \tag{3}$$

where $\mu(t)$ is a fast state vector, $\eta(t)$ is a slow state vector, $\delta(t)$ is the control surface deflection vector, and $y(t)$ is the output vector.

The quality of fast and slow states can be examined by the eigenvalues of the partitioned matrices A_{11} and A_{22}. Since $\mu(t)$ is a fast state vector, then we can write $\|A_{11}\| < \varepsilon \|A_{22}\|$.

In general, an ASE state space model contains both rigid-body modes which usually have low frequencies, and aeroelastic modes which are at much higher frequencies than the rigid-body modes. Flutter modes are usually associated with those aeroelastic modes in the low frequency range. As a result, high frequency aeroelastic modes normally do not participate in a flutter response. In control design, it is usually expedient to remove high-frequency modes in order to simplify a controller design. By removing the high frequency aeroelastic modes, the ASE state space model is reduced in order. Balanced realization is a popular technique for model reduction. In this paper, we will employ a singular perturbation method to reduce the order of an ASE state space model.[7]

Using the singular perturbation approach, the fast and slow dynamics can be decoupled. To decouple the fast and slow states, we perform a time-scale separation by applying the singular perturbation method. Toward that end, we consider a slow time transformation

$$\tau = \varepsilon t \tag{4}$$

where τ is a slow time variable.

Then, the fast and slow state space models are transformed into a singularly perturbed system as

$$\dot{\eta} = A_{11}\eta + A_{12}\mu + B_{11}\delta + B_{12}\dot{\delta} + B_{13}\ddot{\delta} \tag{5}$$

$$\varepsilon\frac{d\mu}{d\tau} = A_{21}\eta + A_{22}\mu + B_{21}\delta + B_{22}\dot{\delta} + B_{23}\ddot{\delta} \tag{6}$$

The Tikhonov's theorem can be used to approximate the solution of the singularly perturbed system with the solution of a "reduced-order" system by setting $\varepsilon = 0$.[8] Thus, the reduced-order system is given by

$$\dot{\eta}_0 = A_{11}\eta_0 + A_{12}\mu_0 + B_{11}\delta + B_{12}\dot{\delta} + B_{13}\ddot{\delta} \tag{7}$$

$$A_{21}\eta_0 + A_{22}\mu_0 + B_{21}\delta + B_{22}\dot{\delta} + B_{23}\ddot{\delta} = 0 \tag{8}$$

where η_0 and μ_0 are the "outer" solution of the singularly perturbed system.

The term "outer" is in connection with the concept of "inner" or "boundary layer" and "outer" solutions which have the origin in boundary layer theory due to Prandtl. The "inner" or "boundary layer" solution for this system is obtained from

$$A_{11}\eta_i + A_{12}\mu_i + B_{11}\delta + B_{12}\dot{\delta} + B_{13}\ddot{\delta} = 0 \tag{9}$$

$$\dot{\mu}_i = A_{21}\eta_i + A_{22}\mu_i + B_{21}\delta + B_{22}\dot{\delta} + B_{23}\ddot{\delta} \tag{10}$$

The solution is then expressed as

$$\eta = \eta_0 + \eta_i - \eta_{MAE} \tag{11}$$

$$\mu = \mu_0 + \mu_i - \mu_{MAE} \tag{12}$$

where $\eta_{MAE}(t)$ and $\mu_{MAE}(t)$ are correction terms by a matched asymptotic expansion method applied to both the inner and outer solutions.[9] The outer solution is in fact the asymptotic solution of the original system as $t \to \infty$.

Since the asymptotic behavior of a closed-loop system is an important consideration for stability implication, the outer solution of the singularly perturbed system is of significant importance. Thus, we obtain the outer solution as

the reduced-order model using only the outer solution of the slow state vector η_0 as

$$\dot{\eta}_0 = \left(\underbrace{A_{11} - A_{12}A_{22}^{-1}A_{21}}_{\bar{A}_{11}}\right)\eta_0 + \left[\underbrace{B_{11} - A_{12}A_{22}^{-1}B_{21}}_{\bar{B}_{11}} \quad \underbrace{B_{12} - A_{12}A_{22}^{-1}B_{22}}_{\bar{B}_{12}} \quad \underbrace{B_{13} - A_{21}A_{22}^{-1}B_{23}}_{\bar{B}_{13}}\right]\begin{bmatrix}\delta\\ \dot{\delta}\\ \ddot{\delta}\end{bmatrix} + \Delta\dot{\eta}_0 \tag{13}$$

$$y = \left(\underbrace{C_1 - C_2A_{22}^{-1}A_{21}}_{\bar{C}_1}\right)\eta_0 + \left(\underbrace{D_1 - C_2A_{22}^{-1}B_{21}}_{\bar{D}_1}\right)\delta + \left(\underbrace{D_2 - C_2A_{22}^{-1}B_{22}}_{\bar{D}_2}\right)\dot{\delta} + \left(\underbrace{D_3 - C_2A_{22}^{-1}B_{23}}_{\bar{D}_3}\right)\ddot{\delta} + \Delta y \tag{14}$$

Now consider a simplified second-order actuator model

$$\ddot{\delta} + 2\zeta\omega_n\dot{\delta} + \omega_n^2\delta = \omega_n^2\delta_c \tag{15}$$

The state space representation then becomes

$$\underbrace{\begin{bmatrix}\dot{\eta}\\ \dot{\delta}\\ \ddot{\delta}\end{bmatrix}}_{\dot{x}} = \underbrace{\begin{bmatrix}\bar{A}_{11} & \bar{B}_{11} - \bar{B}_{13}\omega_n^2 & \bar{B}_{12} - 2\bar{B}_{13}\zeta\omega_n\\ 0 & 0 & I\\ 0 & -\omega_n^2 & -2\zeta\omega_n\end{bmatrix}}_{A}\underbrace{\begin{bmatrix}\eta\\ \delta\\ \dot{\delta}\end{bmatrix}}_{x} + \underbrace{\begin{bmatrix}\bar{B}_{13}\omega_n^2\\ 0\\ \omega_n^2\end{bmatrix}}_{B}\underbrace{\delta_c}_{u} + \underbrace{\begin{bmatrix}\Delta\dot{\eta}\\ 0\\ 0\end{bmatrix}}_{\Delta\dot{x}} \tag{16}$$

$$y = \underbrace{\begin{bmatrix}\bar{C}_1 & \bar{D}_1 - \bar{D}_3\omega_n^2 & \bar{D}_2 - 2\bar{D}_3\zeta\omega_n\end{bmatrix}}_{C}\underbrace{\begin{bmatrix}\eta\\ \delta\\ \dot{\delta}\end{bmatrix}}_{x} + \underbrace{\bar{D}_3\omega_n^2}_{D}\underbrace{\delta_c}_{u} + \Delta y \tag{17}$$

which can be expressed in the canonical form

$$\dot{x} = Ax + Bu \tag{18}$$

$$y = Cx + Du \tag{19}$$

To illustrate the model reduction, ASE state space models at various flight conditions were developed by Boeing Research & Technology under a NASA contract. This model represents the ESAC wing asymmetric modes. The open-loop model has two unstable modes. Using the model reduction method above, it can be shown in Tables 1 that a reduced-order model using only the first 8 modes can capture all the unstable modes and approximate the first 6 modes of the full-order ASE model with 22 modes quite well.

Mode	$n = 6$	$n = 7$	$n = 8$	$n = 22$ (Full)
Rigid	-3.3509	-3.3518	-3.3454	-3.3449
1	-19.9521	-19.7469	-20.0260	-20.0563
2	$4.6884 \pm 21.6354i$	$4.7076 \pm 21.5817i$	$4.6998 \pm 21.6199i$	$4.7027 \pm 21.6211i$
3	$-0.1415 \pm 24.2902i$	$-0.1418 \pm 24.2912i$	$-0.1366 \pm 24.2890i$	$-0.1365 \pm 24.2889i$
4	$-7.0504 \pm 25.8639i$	$-7.0952 \pm 25.8198i$	$-7.427 \pm 26.0338i$	$-7.4493 \pm 26.0608i$
5	$-0.0239 \pm 37.1526i$	$-0.0174 \pm 37.1362i$	$1.2104 \pm 37.5060i$	$1.2643 \pm 37.5538i$

Table 2 - Asymmetric Modes @ Mach 0.86 and 0 ft (VCCTEF_PT_AS_Mp86_H00.mat)

Mode	$n=6$	$n=7$	$n=8$	$n=22$ (Full)
Rigid	-2.7392	-2.7395	-2.7385	-2.7385
1	$2.7294 \pm 19.8683i$	$2.7512 \pm 19.8529i$	$2.7804 \pm 19.8561i$	$2.7842 \pm 19.8513i$
2	$-0.1553 \pm 24.3565i$	$-0.1557 \pm 24.3562i$	$-0.1547 \pm 24.3553i$	$-0.1549 \pm 24.3552i$
3	$-6.3434 \pm 24.0892i$	$-6.3272 \pm 24.0739i$	$-6.4220 \pm 23.9949i$	$-6.4174 \pm 23.9920i$
4	$-0.3902 \pm 37.1580i$	$-0.3782 \pm 37.1461i$	$0.0571 \pm 37.4423i$	$0.0584 \pm 37.4846i$
5	$-20.0160 \pm 32.3722i$	$-20.2813 \pm 32.3013i$	$-20.4217 \pm 32.4999i$	$-20.4833 \pm 32.5445i$

Table 3 - Asymmetric Modes @ Mach 0.86 and 10,000 ft (VCCTEF_PT_AS_Mp86_H10.mat)

Mode	$n=6$	$n=7$	$n=8$	$n=22$ (Full)
Rigid	-2.0746	-2.0747	-2.0745	-2.0745
1	$0.7903 \pm 18.1375i$	$0.8018 \pm 18.1385i$	$0.8171 \pm 18.1481i$	$0.8198 \pm 18.1459i$
2	$-4.4641 \pm 20.4767i$	$-4.4687 \pm 20.4764i$	$-4.4906 \pm 20.4657i$	$-4.4900 \pm 20.4700i$
3	$-0.1751 \pm 24.4220i$	$-0.1749 \pm 24.4218i$	$-0.1748 \pm 24.4211i$	$-0.1748 \pm 24.4210i$
4	$-1.2718 \pm 36.9051i$	$-1.2528 \pm 36.9020i$	$-1.1653 \pm 37.1472i$	$-1.1782 \pm 37.1724i$
5	$-9.9580 \pm 41.9817i$	$-10.0850 \pm 41.9660i$	$-10.1183 \pm 41.8219i$	$-10.1254 \pm 41.8270i$

Table 4 - Asymmetric Modes @ Mach 0.86 and 20,000 ft (VCCTEF_PT_AS_Mp86_H20.mat)

Mode	$n=6$	$n=7$	$n=8$	$n=22$ (Full)
Rigid	-1.4746	-1.4747	-1.4747	-1.4747
1	$-0.8119 \pm 15.3391i$	$-0.8116 \pm 15.3423i$	$-0.8132 \pm 15.3481i$	$-0.8119 \pm 15.3485i$
2	$-1.5973 \pm 20.3657i$	$-1.5961 \pm 20.3629i$	$-1.6023 \pm 20.3599i$	$-1.6030 \pm 20.3603i$
3	$-0.1667 \pm 24.4533i$	$-0.1667 \pm 24.4533i$	$-0.1669 \pm 24.4531i$	$-0.1669 \pm 24.4530i$
4	$-1.4328 \pm 35.9317i$	$-1.4290 \pm 35.9368i$	$-1.4601 \pm 36.0166i$	$-1.4701 \pm 36.0234i$
5	$-5.7255 \pm 46.4733i$	$-5.7766 \pm 46.4699i$	$-5.7264 \pm 46.4024i$	$-5.7217 \pm 46.4071i$

Table 5 - Asymmetric Modes @ Mach 0.86 and 30,000 ft (VCCTEF_PT_AS_Mp86_H30.mat)

III. Linear Quadratic Gaussian Optimal Control Modification

The linear quadratic gaussian (LQG) is a standard technique for control design of systems with output or partial state information. A state observer is constructed using the Kalman filter optimal estimation method as

$$\dot{\hat{x}} = A\hat{x} + L(y - \hat{y}) + Bu \tag{20}$$

where $\hat{x}$ is the estimated state vector, L is the Kalman filter gain, and $\hat{y}$ is the estimated output

$$\hat{y} = C\hat{x} + Du \tag{21}$$

The objective is to design a closed-loop observer model that tracks a reference model

$$\dot{x}_m = A_m x_m + B_m r \tag{22}$$

Consider an ideal controller

$$u^* = K_x^* \hat{x} + K_y^* (y - \hat{y}) + K_r^* r \tag{23}$$

The ideal closed-loop observer model is then expressed

$$\dot{\hat{x}} = A\hat{x} + L(y - \hat{y}) + BK_x^* \hat{x} + BK_y^* (y - \hat{y}) + BK_r^* r \tag{24}$$

Assuming the following model matching conditions are satisfied

$$A + BK_x^* = A_m \tag{25}$$

$$BK_r^* = B_m \tag{26}$$

$$BK_y^* = -L \tag{27}$$

Then the adaptive controller is designed as

$$u = K_x(t)\hat{x} + K_y(t)(y - \hat{y}) + K_r(t) r \tag{28}$$

Let $\tilde{K}_x = K_x - K_x^*$, $\tilde{K}_y = K_y - K_y^*$, $\tilde{K}_r = K_r - K_r^*$ be the estimation errors of $K_x(t)$, $K_y(t)$, and $K_r(t)$. Then the closed-loop plant is written as

$$\dot{\hat{x}} = A_m \hat{x} + B_m r + B\tilde{K}_x \hat{x} + B\tilde{K}_y (y - \hat{y}) + B\tilde{K}_r r \tag{29}$$

Let $e = x_m - \hat{x}$ be the tracking error, then the equation is expressed as

$$\dot{e} = A_m e - B\tilde{K}_x \hat{x} - B\tilde{K}_y (y - \hat{y}) - B\tilde{K}_r r \tag{30}$$

The adaptive laws for $K_x(t)$, $K_y(t)$, and $K_r(t)$ using the optimal control modification[10,11] are given by

$$\dot{K}_x^\top = \Gamma_x \hat{x} \left(e^\top P + \nu_x \hat{x}^\top K_x^\top B^\top P A_m^{-1} \right) B \tag{31}$$

$$\dot{K}_y^\top = \Gamma_y (y - \hat{y}) \left[e^\top P + \nu_y (y - \hat{y})^\top K_y^\top B^\top P A_m^{-1} \right] B \tag{32}$$

$$\dot{K}_r^\top = \Gamma_r r \left(e^\top P + \nu_r r^\top K_r^\top B^\top P A_m^{-1} \right) B \tag{33}$$

with the initial conditions $K_x(0) = \bar{K}_x$, $K_y(0) = \bar{K}_y$, and $K_r(0) = \bar{K}_r$, where $\Gamma_x = \Gamma_x^\top > 0$, $\Gamma_y = \Gamma_y^\top > 0$, and $\Gamma_r = \Gamma_r^\top > 0$ are the adaptive gains, $\nu_x > 0$ $\nu_y > 0$, and $\nu_r > 0$ are the modification parameters, and $P = P^\top > 0$ is the solution of the Lyapunov equation

$$PA_m + A_m^\top P + Q = 0 \tag{34}$$

where $Q = Q^\top > 0$.

For an adaptive augmentation regulator design whereby the reference model is zero, the adaptive controller is given by

$$u = \bar{K}_x \hat{x} + \Delta K_x \hat{x} + K_y (y - \hat{y}) \tag{35}$$

where $\bar{K}_x$ is obtained from the linear quadratic regulator (LQR) design of the full-state equation, and the adaptive laws for $\Delta K_x(t)$ and $K_y(t)$ are given by

$$\Delta\dot{K}_x^\top = -\Gamma_x \hat{x}\hat{x}^\top \left(P - \nu_x \Delta K_x^\top B^\top P A_m^{-1}\right) B \tag{36}$$

$$\dot{K}_y^\top = -\Gamma_y (y-\hat{y}) \left[\hat{x}^\top P - \nu_y (y-\hat{y})^\top K_y^\top B^\top P A_m^{-1}\right] B \tag{37}$$

The adaptive laws can be shown to be stable as follows:

Choose a Lyapunov candidate function

$$V = \hat{x}^\top P \hat{x} + \text{trace}\left(\Delta\tilde{K}_x \Gamma_x^{-1} \Delta\tilde{K}_x^\top\right) + \text{trace}\left(\tilde{K}_y \Gamma_y^{-1} \tilde{K}_y^\top\right) \tag{38}$$

Evaluating $\dot{V}$ yields

$$\dot{V} = -\hat{x}^\top Q \hat{x} + 2\nu_x \hat{x}^\top \Delta K_x^\top B^\top P A_m^{-1} B \Delta\tilde{K}_x \hat{x} + 2\nu_y (y-\hat{y})^\top K_y^\top B^\top P A_m^{-1} B \tilde{K}_y (y-\hat{y}) \tag{39}$$

Note that $PA_m^{-1} = M + N$

$$M = \frac{1}{2}\left(PA_m^{-1} + A_m^{-\top} P\right) = -\frac{1}{2} A_m^{-\top} Q A_m^{-1} < 0 \tag{40}$$

$$N = \frac{1}{2}\left(PA_m^{-1} - A_m^{-\top} P\right) \tag{41}$$

$N = -N^\top$ which implies $z^\top N z = 0$. Therefore

$$\begin{aligned}\dot{V} = &-\hat{x}^\top Q \hat{x} - \nu_x \hat{x}^\top \Delta\tilde{K}_x^\top B^\top A_m^{-\top} Q A_m^{-1} B \Delta\tilde{K}_x \hat{x} - \nu_y (y-\hat{y})^\top \tilde{K}_y^\top B^\top A_m^{-\top} Q A_m^{-1} B \tilde{K}_y (y-\hat{y}) \\ &+ 2\nu_x \hat{x}^\top \Delta K_x^{*\top} B^\top P A_m^{-1} B \Delta\tilde{K}_x \hat{x} + 2\nu_y (y-\hat{y})^\top K_y^{*\top} B^\top P A_m^{-1} B \tilde{K}_y (y-\hat{y})\end{aligned} \tag{42}$$

$\dot{V}$ is then bounded by

$$\dot{V} \le -c_1 \|\hat{x}\|^2 - \nu_x c_2 \|\hat{x}\|^2 \left(\left\|\Delta\tilde{K}_x\right\| - c_3 \|\Delta K_x^*\|\right)^2 - \nu_y c_2 \|y-\hat{y}\|^2 \left(\left\|\tilde{K}_y\right\| - c_3 \left\|K_y^*\right\|\right)^2 \tag{43}$$

$$+ \nu_x c_2 c_3^2 \|\hat{x}\|^2 \|\Delta K_x^*\|^2 + \nu_y c_2 c_3^2 \|y-\hat{y}\|^2 \left\|K_y^*\right\|^2 \tag{44}$$

where $c_1 = \lambda_{min}(Q)$, $c_2 = \lambda_{min}\left(B^\top A_m^{-\top} Q A_m^{-1} B\right)$, and $c_3 = \frac{\left\|B^\top P A_m^{-1} B\right\|}{c_2}$.

Then $\dot{V} \le 0$ if

$$\|\hat{x}\| \ge c_3 \|y-\hat{y}\| \left\|K_y^*\right\| \sqrt{\frac{\nu_y c_2}{c_1 - \nu_x c_2 c_3^2 \|\Delta K_x^*\|^2}} = \rho \tag{45}$$

$$\left\|\Delta\tilde{K}_x\right\| \ge c_3 \|\Delta K_x^*\| + \sqrt{c_3^2 \|\Delta K_x^*\|^2 + \frac{\nu_y c_3^2 \|y-\hat{y}\|^2 \left\|K_y^*\right\|^2}{\nu_x \|\hat{x}\|^2}} = \kappa \tag{46}$$

$$\left\|\tilde{K}_y\right\| \ge c_3 \left\|K_y^*\right\| + \sqrt{c_3^2 \left\|K_y^*\right\|^2 + \frac{\nu_x c_3^2 \|\hat{x}\|^2 \|\Delta K_x^*\|^2}{\nu_y \|y-\hat{y}\|^2}} = \sigma \tag{47}$$

In addition, we require that $c_1 - \nu_x c_2 c_3^2 \|\Delta K_x^*\|^2 > 0$ which implies $\nu_x < \frac{c_1}{c_2 c_3^2 \|\Delta K_x^*\|^2}$. Then, all signals are uniformly

ultimately bounded with an ultimate bound

$$\lim_{t\longrightarrow\infty}\|\hat{x}\| \leq \sqrt{\frac{\lambda_{max}(P)\,\rho^2+\lambda_{max}\left(\Gamma_x^{-1}\right)\kappa^2+\lambda_{max}\left(\Gamma_y^{-1}\right)\sigma^2}{\lambda_{min}(P)}} \tag{48}$$

Thus, the adaptive optimal control modification regulator does not result in $\hat{x}(t)\rightarrow 0$ as $t\rightarrow\infty$. This is because the optimal control modification provides robustness by seeking a optimal solution of $\hat{x}(t)$ bounded away from the origin. The proximity of $\hat{x}(t)$ can be controlled by the modification parameters ν_x and ν_y. By setting $\nu_x = 0$ and $\nu_y = 0$, we recover the standard model reference adaptive control which results in $\hat{x}(t)\rightarrow 0$ as $t\rightarrow\infty$. However, the MRAC regulator is proven to be non-robust in presence of disturbance which will cause parameter drift. Thus, it is not advisable to use standard MRAC for adaptive regulator design.

The optimal control modification has a linear limiting property under fast adaptation with large adaptive gains.[12] In the theoretical limit as $\Gamma\rightarrow\infty$, then

$$B\Delta K_x \rightarrow \frac{1}{\nu_x}B\left(B^\top A_m^{-\top}PB\right)^{-1}B^\top P \tag{49}$$

$$BK_y y \rightarrow \frac{1}{\nu_y}B\left(B^\top A_m^{-\top}PB\right)^{-1}B^\top P\hat{x} \tag{50}$$

Using this limiting property, it is possible to estimate stability margin of the closed-loop system in the limit, which becomes

$$\dot{x} = Ax + B\bar{K}_x\hat{x} + \left(\frac{1}{\nu_x}+\frac{1}{\nu_y}\right)B\left(B^\top A_m^{-\top}PB\right)^{-1}B^\top P\hat{x} \tag{51}$$

$$\dot{\hat{x}} = \left[A + B\bar{K}_x + \left(\frac{1}{\nu_x}+\frac{1}{\nu_y}\right)P^{-1}A_m^\top P - LC\right]\hat{x} + LCx \tag{52}$$

Thus the closed-loop matrix is given by

$$A_c = \begin{bmatrix} A & B\bar{K}_x + \left(\frac{1}{\nu_x}+\frac{1}{\nu_y}\right)B\left(B^\top A_m^{-\top}PB\right)^{-1}B^\top P \\ LC & A - LC + B\bar{K}_x + \left(\frac{1}{\nu_x}+\frac{1}{\nu_y}\right)B\left(B^\top A_m^{-\top}PB\right)^{-1}B^\top P \end{bmatrix} \tag{53}$$

Then, ν_x and ν_y can be chosen to provide stability margin based on the closed-loop poles.

IV. Implementation

The ASE state space model contains 45 states using p-transform without unsteady aerodynamic lag states, 64 outputs, and 4 inputs. The states include one rigid-body state; namely the aircraft roll rate p, and two generalized states for each of the 22 aeroelastic modes. The outputs include the aircraft airspeed V_∞, angle of attack α, sideslip angle β, aircraft angular rates (p,q,r), aircraft position (x,y,z), aircraft attitude (ϕ,θ,ψ), accelerations in three axes (N_x,N_y,N_z) at forward of wing tip, aft of wing tip, wing root centerline, and engine center of gravity, and the four hinge moments of the control surfaces. The inputs are the four outboard third camber segments of the VCCTEF.

For the flutter suppression control design, the two N_z acceleration measurements are used at outputs. Figure 7 illustrates the input and output locations.

All the control surfaces are not entirely independent in their motions due to the physical constraints imposed by the elastomer transition material. This material has certain position and rate limits. Thus, the control surfaces will have relative position and rate limits. These limits are not the normal position and rate limits that actuators are subjected to.

Thus, these relative constraints can cause challenges in a control design of this system.

Consider the following relative constraints

$$|\delta_{i+1} - \delta_i| \leq \Delta\delta \tag{54}$$

$$\left|\dot{\delta}_{i+1} - \dot{\delta}_i\right| \leq \Delta\dot{\delta} \tag{55}$$

where $i = 1, 2, 3$.

For the VCCTEF design, the relative motion between any pair of adjacent flap sections is allowed to be within 2 degrees. The rate constraint imposed by the elastomer material is not yet defined and thus is assumed to be large. The actuator dynamics are modeled as a second-order system. This actuator model is highly simplified since it does not take into account the hinge moment which is a function of the states and the dynamics of the elastomer material which contributes mass, damping, and stiffness to the overall actuator model. In the future, a detail actuator model of the VCCTEF will be developed.

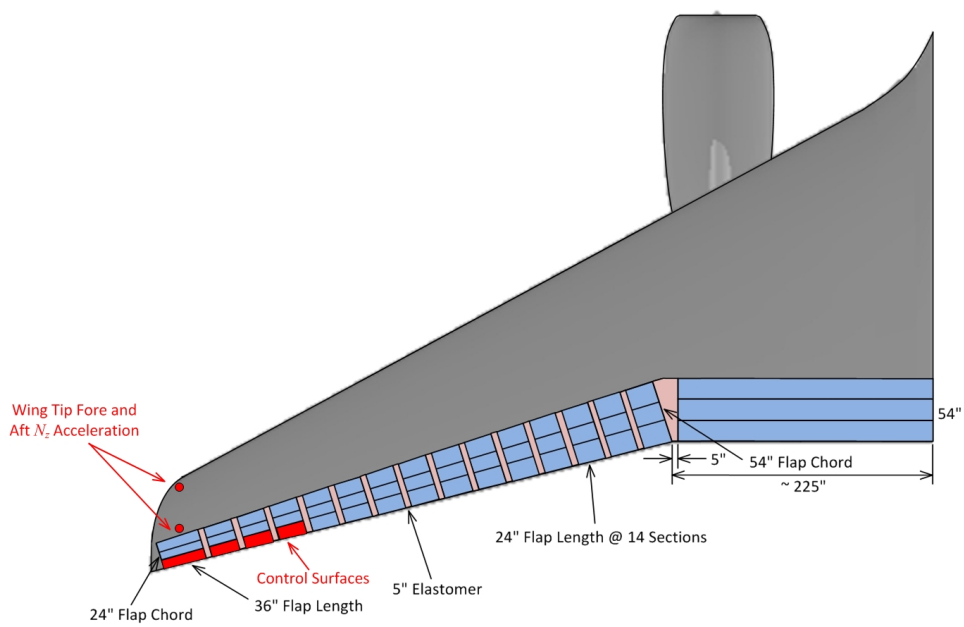

Fig. 7 - Flutter Suppression Input and Output Locations

To address the relative position limit, a concept of virtual control has recently been introduced.[13] The control surface deflections are described by a shape function. This shape function can be any reasonable shape function with a smooth and gradual slope. One simple function is a linear function. The control surface deflections are then parametrized as a linear function

$$\delta_i = \frac{i\delta_v}{4} \tag{56}$$

where $i = 1, 2, 3, 4$ such that δ_1 is the inboard flap and δ_4 is the outboard flap, and δ_v is the virtual control surface deflection.

Since the inboard flap section δ_1 cannot deflect more than 2 degrees relative to the stationary flap adjacent to it, then $\delta_v \leq 8$ deg. Also, the outboard flap deflection δ_4 is the same as the virtual control surface deflection. Thus, one can think that outboard flap δ_4 is a master control input while the other three control surfaces are slave control inputs since their motions are dependent on the master control input.

Thus, the virtual control derivatives are computed as

$$B_{jk} = \sum_{i=1}^{4} \frac{iB_{jk_i}}{4} \tag{57}$$

where B_{jk_i} is the control derivative of mode j-th with respect to the displacement $(k = 1)$, velocity $(k = 2)$, and acceleration $(k = 3)$ of flap section i-th.

The simulation is conducted with only the reduced-order aeroservoelastic state space model for flight condition at Mach 0.86 and altitude of 10,000 ft. There are two unstable aeroelastic modes: mode 1 and mode 4, as shown in Table 3. Process noise and sensor noise are introduced to simulate the structural response to atmospheric turbulence. The baseline full-state feedback controller is designed with an LQR controller tuned to give good performance. An LQG output feedback controller is then designed using the ideal full-state feedback gain. The adaptive augmentation controller is then turned on. The adaptive gain matrices and modification parameters are selected to be $\Gamma_x = \Gamma_y = 1$ and $\eta_x = \eta_y = 0.1$.

The root locus of the open-loop transfer functions between the accelerometers and the virtual control are shown in Figs. 8 and 9. It can be seen that the transfer functions are unstable and non-minimum phase with zeros on the right half plane. This non-minimum phase behavior can be challenging for adaptive control.

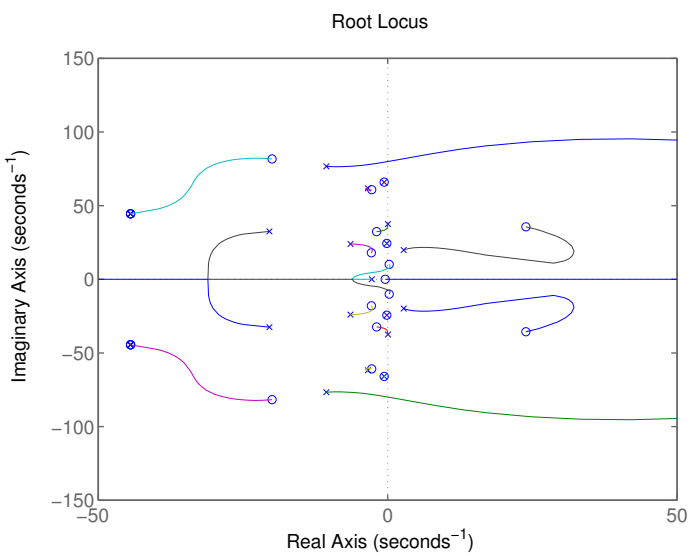

Fig. 8 - Root Locus of Open-Loop Transfer Function of Forward Accelerometer

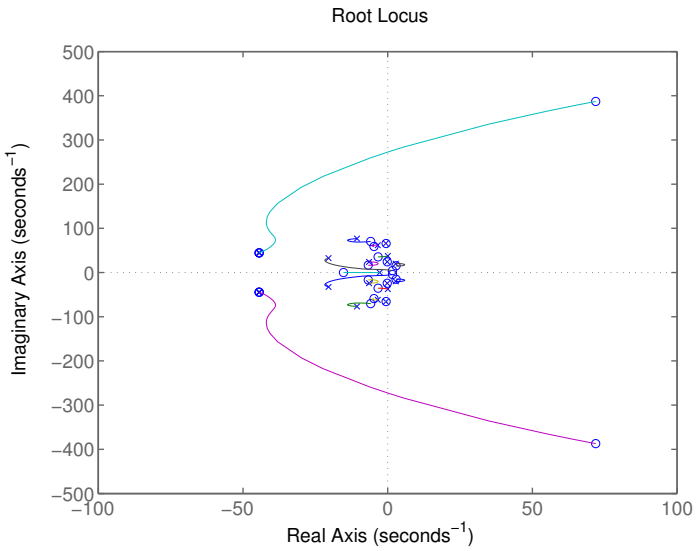

Fig. 9 - Root Locus of Open-Loop Transfer Function of Aft Accelerometer

An initial rol rate of 0.1 rad/sec is specified. Figures 10, 11, and 12 show the responses of the roll rate, the generalized displacement of mode 1, and the generalized displacement of mode 4 without process and sensors noises for the baseline full-state feedback LQR controller and the output feedback LQG controller with and without the adaptive augmentation controller. The full-state feedback LQR controller performs much better than the output feedback LQG controller with and without the adaptive augmentation controller using only the two accelerometers at the wing tip. The adaptive augmentation controller causes an increase in the overshoot of the responses due to the output feedback LQG controller as well as injects high frequency contents into the modal responses. Nonetheless, all the controllers are able to suppress the two unstable aeroelastic modes.

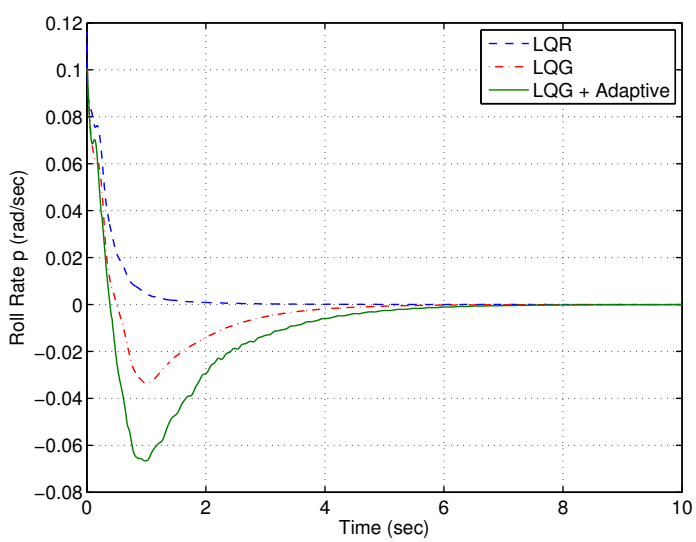

Fig. 10 - Roll Rate Response for LQR and LQG Controllers without Process and Sensor Noises

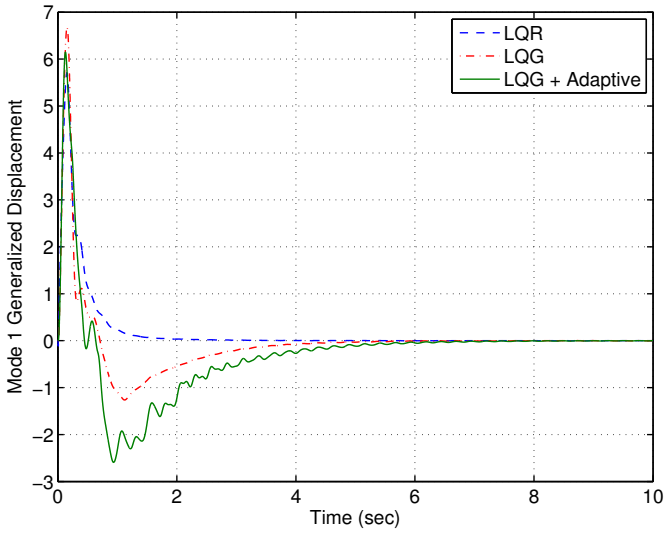

Fig. 11 - Mode 1 Generalized Displacement Response for LQR and LQG Controllers without Process and Sensor Noises

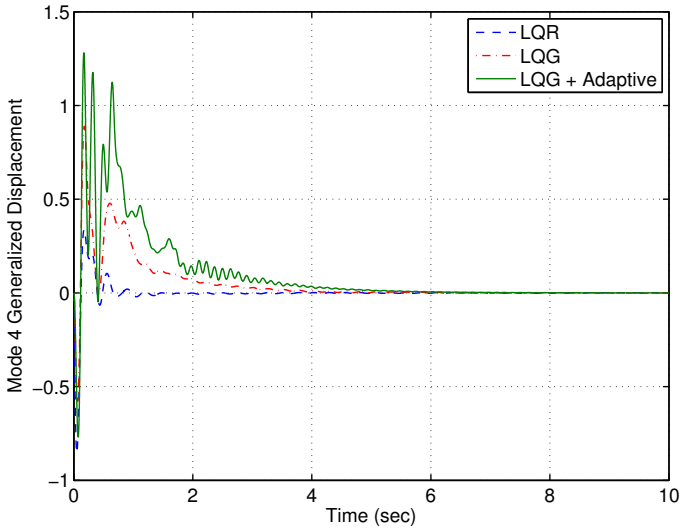

Fig. 12 - Mode 4 Generalized Displacement Response for LQR and LQG Controllers without Process and Sensor Noises

The effects of process and sensor noises are examined. Figures 13, 14, and 15 show the responses of the roll rate, the generalized displacement of mode 1, and the generalized displacement of mode 4 with process and sensor noises for the baseline full-state feedback LQR controller and the output feedback LQG controller with and without the adaptive augmentation controller. All the controllers are able to maintain good performance in the presence of process and sensor noises.

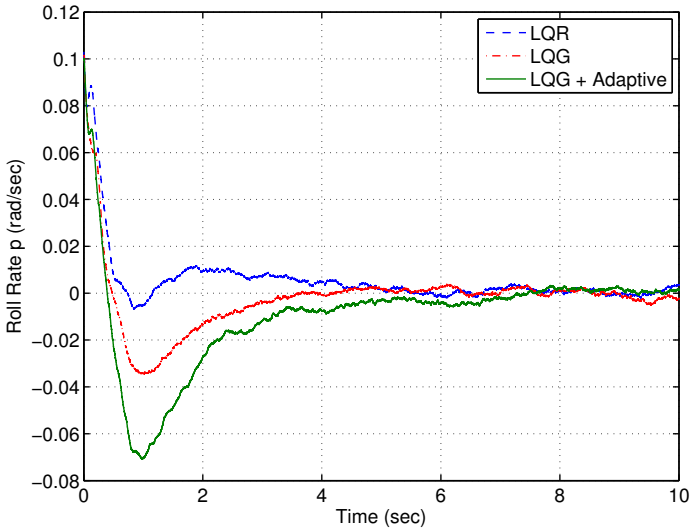

Fig. 13 - Roll Rate Response for LQR and LQG Controllers with Process and Sensor Noises

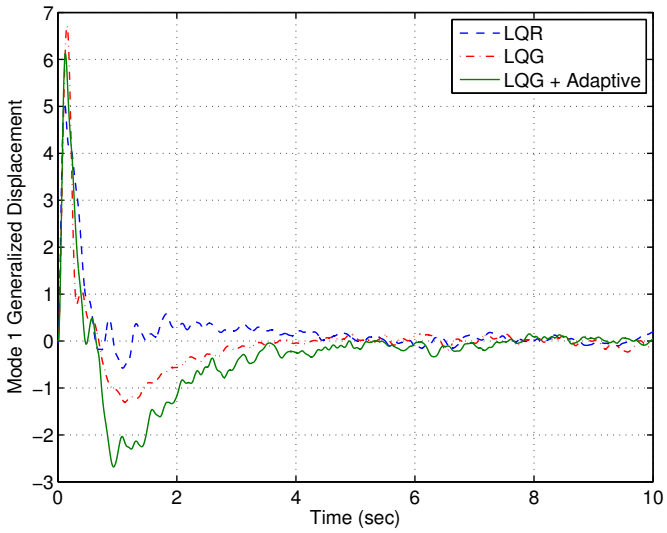

Fig. 14 - Mode 1 Generalized Displacement Response for LQR and LQG Controllers with Process and Sensor Noises

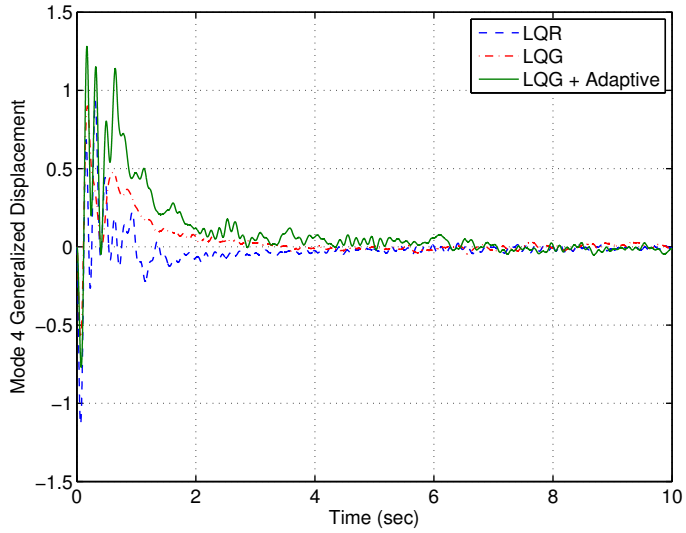

Fig. 15 - Mode 4 Generalized Displacement Response for LQR and LQG Controllers with Process and Sensor Noises

Figures 16 and 17 show the root locus plots of the closed-loop transfer functions of the accelerometers with the adaptive augmentation controller using the final gain matrix. As can be seen, the closed-loop transfer functions are completely stable. Figures 18 and 19 are the frequency response plots for the open-loop and closed-loop transfer functions of the accelerometers. The largest frequency response is due to mode 4. The closed-loop frequency response is significantly less than the open-loop frequency response, indicating the effectiveness of the aeroelastic mode suppression controller.

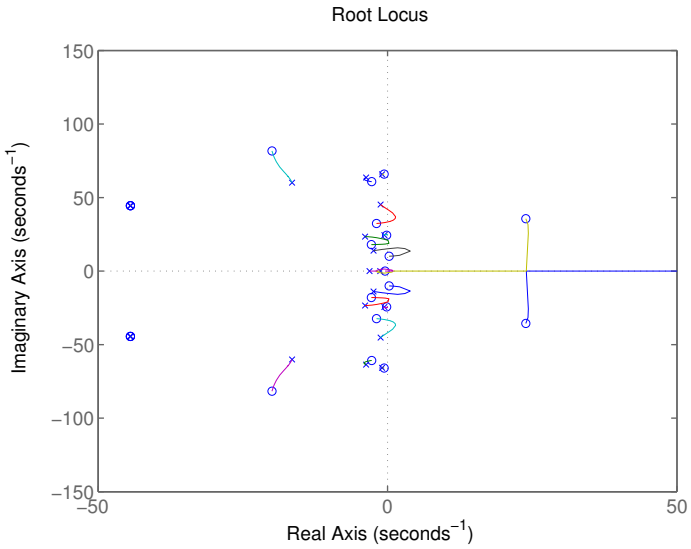

Fig. 16 - Root Locus of Closed-Loop Transfer Function of Forward Accelerometer

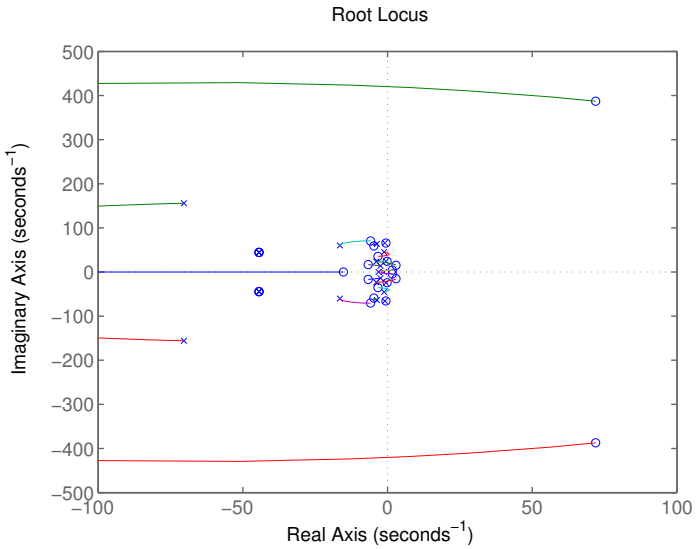

Fig. 17 - Root Locus of Closed-Loop Transfer Function of Aft Accelerometer

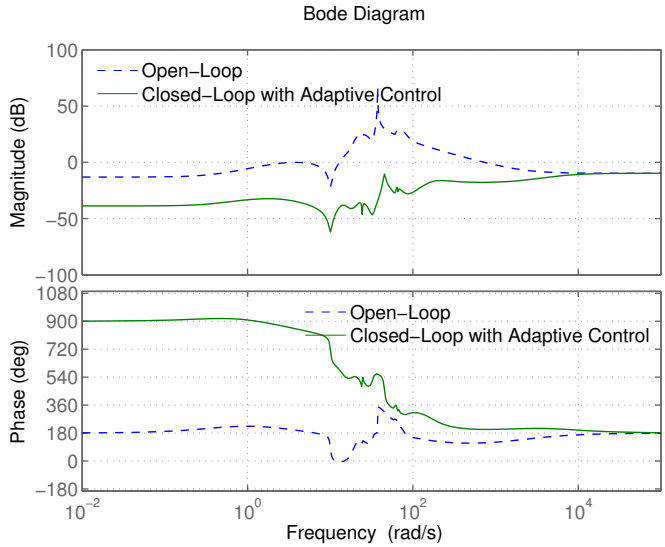

Fig. 18 - Frequency Response of Forward Accelerometer

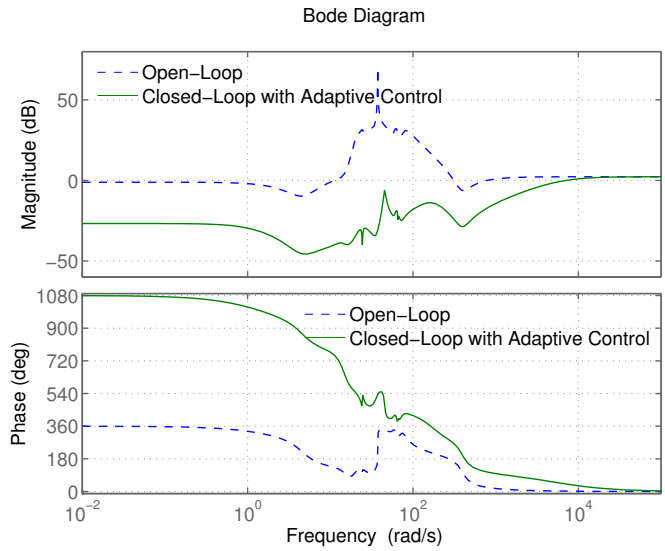

Fig. 19 - Frequency Response of Aft Accelerometer

Next, uncertainty is introduced into the aeroservoelastic state space model by $\Delta A = 0.05A$ and $\Delta B = -0.1B$. Process and sensor noises are also included. The output feedback LQG controller without the adaptive augmentation controller is unstable as shown in Figs. 20, 21, and 22. The figures also show that the adaptive augmentation controller is able to stabilize the aeroelastic modes in the presence of the uncertainty.

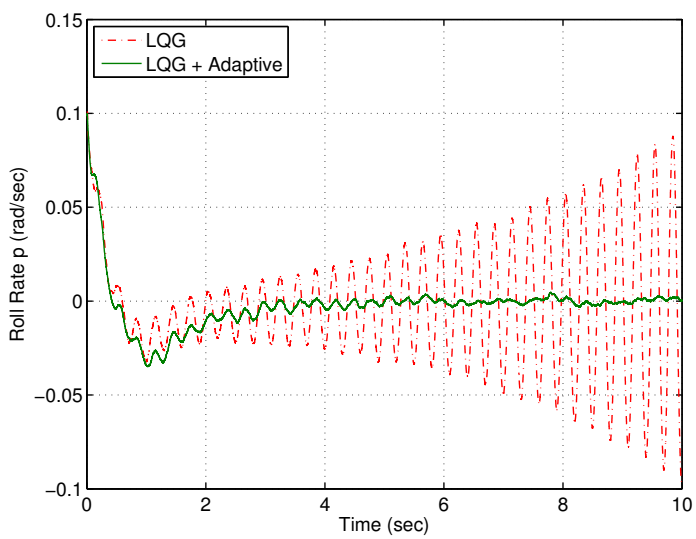

Fig. 20 - Roll Rate Response with and without Adaptive Augmentation Controller

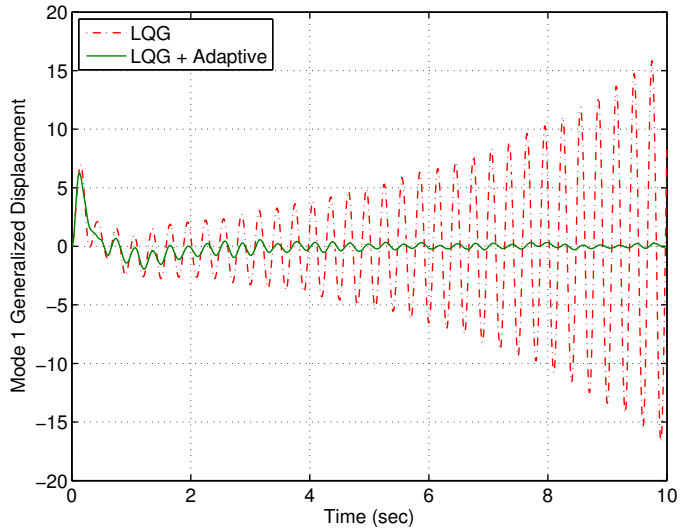

Fig. 21 - Mode 1 Generalized Displacement Response with and without Adaptive Augmentation Controller

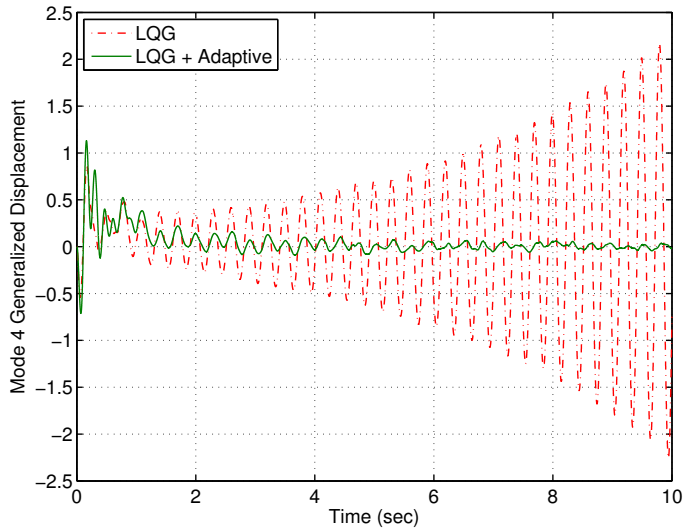

Fig. 22 - Mode 4 Generalized Displacement Response with and without Adaptive Augmentation Controller

Figure 23 is the plot of the time history of the virtual control command for the output feedback LQG controller with and without the adaptive augmentation controller. The largest amplitude of the stabilizing virtual control command for the adaptive augmentation controller is 6.22^{o}. The linear mapping between the virtual control command and the physical control commands result in 1.56^{o} which meets the physical constraints of 2° on the relative deflection of the VCCTEF.

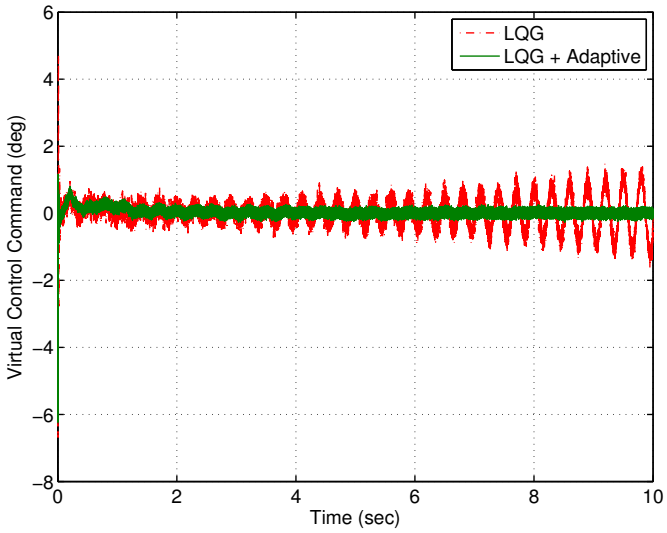

Fig. 23 - Virtual Control Command with and without Adaptive Augmentation Controller

V. Discussion

It should be noted that the simulation study is limited in scope. It would be of interest to see how an adaptive controller could be designed to stabilize the unstable aeroelastic modes at two points in the flight envelope. This could enable a gain-scheduling control strategy using adaptive control. Also, the aeroservoelastic state space model developed by Boeing is based on a frequency-dependent p-transform solution. So the state space model is only valid at a given frequency which in this case is the flutter frequency of mode 1. Since there are two unstable modes, the behavior of mode 4 may not be accurately captured in the model. Furthermore, the closed-loop frequency could potentially be different from the open-loop flutter frequency. This could render the control design invalid. In the future, we will be using a more detail aeroservoelastic state space model developed by NASA which uses aerodynamic lag states to approximate the unsteady aerodynamic effect over a wider range of frequencies.

Flexible structures in general can introduce a non-minimum phase behavior in an output feedback control design. This non-minimum phase behavior can challenge adaptive output feedback control. As a result, adaptive gain must be designed to be properly bounded. This generally would require having a priori knowledge of the unstable zeros. In some way, robustness of adaptive control for a non-minimum phase plant is difficult to be established without knowing the behavior of the plant.

VI. Conclusion

This paper presents a method of augmenting an output feedback linear quadratic Gaussian regulator controller with an adaptive augmentation controller using the optimal control modification method. The method is applied to a flutter suppression control for a flexible wing aircraft with a novel control device called the Variable Camber Continuous Trailing Edge Flap (VCCTEF). The aeroservoelastic state space model contains 22 modes. A model reduction is performed using a singular perturbation approach. The reduced-order aeroservoelastic state space model approximates the unstable modes quite well with only the first 8 modes. A simulation is performed to assess the effectiveness of the adaptive augmentation control design using the reduced-order model. Process and sensor noises

are included in the model to provide realistic simulations. A virtual control is used to address the physical constraints on the relative deflection of the VCCTEF imposed by the elastomer materials. Simulation results indicate that the adaptive augmentation control design is effective in suppressing unstable aeroelastic modes.

Acknowledgment

The authors would like to thank the Fixed Wing / Advanced Air Transport Technology Project under the Fundamental Aeronautics Program of NASA Aeronautics Research Mission Directorate (ARMD) for funding support of this work. The authors also would like to acknowledge Boeing Research and Technology for their collaboration with NASA under NASA contract NNL12AD09T entitled "Development of Variable Camber Continuous Trailing Edge Flap System for B757 Configured with a More Flexible Wing."

References

[1]Nguyen, N., "Elastically Shaped Future Air Vehicle Concept," NASA Innovation Fund Award 2010 Report, October 2010, Submitted to NASA Innovative Partnerships Program, http://ntrs.nasa.gov/archive/nasa/casi.ntrs.nasa.gov/20110023698.pdf

[2]Nguyen, N., Trinh, K., Reynolds, K., Kless, J., Aftosmis, M., Urnes, J., and Ippolito, C., "Elastically Shaped Wing Optimization and Aircraft Concept for Improved Cruise Efficiency," AIAA Aerospace Sciences Meeting, AIAA-2013-0141, January 2013.

[3]Boeing Report No. 2012X0015, "Development of Variable Camber Continuous Trailing Edge Flap System," October 4, 2012.

[4]Urnes, J., Nguyen, N., Ippolito, C., Totah, J., Trinh, K., and Ting, E., "A Mission Adaptive Variable Camber Flap Control System to Optimize High Lift and Cruise Lift to Drag Ratios of Future N+3 Transport Aircraft," AIAA Aerospace Sciences Meeting, AIAA-2013-0214, January 2013.

[5]Nguyen, N, Precup, N., Urnes, J., Nelson, C., Lebofsky, S., Ting, E., and Livne, E., "Experimental Investigation of a Flexible Wing with a Variable Camber Continuous Trailing Edge Flap Design," 32nd AIAA Applied Aerodynamics Conference, AIAA-2014-2442, June 2014.

[6]Nguyen, N., Ting, E., Nguyen, D., Trinh, K., "Flutter Analysis of Mission-Adaptive Wing with Variable Camber Continuous Trailing Edge Flap," 55th AIAA/ASME/ASCE/AHS/ASC Structures, Structural Dynamics, and Materials Conference, AIAA-2014-0839, January 2014.

[7]Nguyen, N. and Tal, E., "A Multi-Objective Flight Control Approach for Performance Adaptive Aeroelastic Wing," 56th AIAA/ASME/ASCE/AHS/ASC Structures, Structural Dynamics, and Materials Conference, AIAA-2015-1843, January 2015.

[8]Kokotovic, P., Khalil, H., and O'Reilly, J., *Singular Perturbation Methods in Control: Analysis and Design*, Society for Industrial and Applied Mathematics, 1987.

[9]Ardema, M., "Computational Singular Perturbation Method for Dynamical Systems", AIAA Journal of Guidance, Control, and Dynamics, Vol. 14, 661-663, 1981.

[10]Nguyen, N., "Optimal Control Modification for Robust Adaptive Control with Large Adaptive Gain," *Systems & Control Letters*, 61 (2012) pp. 485-494.

[11]Nguyen, N., Krishnakumar, K., and Boskovic, J., "An Optimal Control Modification to Model Reference Adaptive Control for Fast Adaptation," AIAA Guidance, Navigation, and Control Conference, AIAA-2008-7283, August 2008.

[12]Nguyen, N., "Adaptive Control for Linear Uncertain Systems with Unmodeled Dynamics Revisited via Optimal Control Modification," AIAA Guidance, Navigation, and Control Conference, AIAA-2013-4988, August 2013.

[13]Nguyen, N. and Urnes, J., "Aeroelastic Modeling of Elastically Shaped Aircraft Concept via Wing Shaping Control for Drag Reduction," AIAA Atmospheric Flight Mechanics Conference, AIAA-2012-4642, August 2012.